Anomalous Fraunhofer-like patterns in quantum anomalous Hall Josephson junctions

Junjie Qi [1,*] Haiwen Liu,[2] Jie Liu,[3] Hua Jiang,[4] Dong E. Liu,[1,5,6,7] Chui-Zhen Chen,[8,9,†] Ke He [1,5,6,7] and X. C. Xie[4,7,10]

[1]*Beijing Academy of Quantum Information Sciences, Beijing 100193, China*
[2]*Center for Advanced Quantum Studies, Department of Physics, Beijing Normal University, Beijing 100875, China*
[3]*School of Physics, Xi'an Jiaotong University, Ministry of Education Key Laboratory for Non-Equilibrium Synthesis and Modulation of Condensed Matter, Xi'an 710049, China*
[4]*Institute for Nanoelectronic Devices and Quantum Computing, Fudan University, Shanghai 200433, China*
[5]*State Key Laboratory of Low Dimensional Quantum Physics, Department of Physics, Tsinghua University, Beijing 100084, China*
[6]*Frontier Science Center for Quantum Information, Beijing 100084, China*
[7]*Hefei National Laboratory, Hefei 230088, China*
[8]*School of Physical Science and Technology, Soochow University, Suzhou 215006, China*
[9]*Institute for Advanced Study, Soochow University, Suzhou 215006, China*
[10]*International Center for Quantum Materials, School of Physics, Peking University, Beijing 100871, China*

The intriguing interplay between topology and superconductivity has attracted significant attention, given its potential for realizing topological superconductivity. In the quantum anomalous Hall insulators (QAHIs)-based junction, the supercurrents are carried by the chiral edge states, characterized by a $2\Phi_0$ magnetic flux periodicity ($\Phi_0 = h/2e$ is the flux quantum, h the Planck constant, and e the electron charge). However, experimental observations indicate the presence of bulk carriers in QAHI samples due to magnetic dopants. In this study, we reveal a systematic transition from edge-state to bulk-state dominant supercurrents as the chemical potential varies from the bulk gap to the conduction band. This results in an evolution from a $2\Phi_0$-periodic oscillation pattern to an asymmetric Fraunhofer pattern. Furthermore, a Fraunhoher-like pattern emerges due to the coexistence of chiral edge states and bulk states caused by magnetic domains, even when the chemical potential resides within the gap. These findings not only advance the theoretical understanding but also pave the way for the experimental discovery of the chiral Josephson effect based on QAHI doped with magnetic impurities.

I. INTRODUCTION

In recent decades, research on quantum anomalous Hall insulators (QAHIs) has flourished, driven not only by the intriguing physical phenomena they exhibit but also by their potential for various technological applications [1–4]. These applications include serving as platforms for realizing topological quantum computation, resistance standards, and dissipation-free interconnects [3]. In a QAHI, the bulk behaves as an insulator, while electrons can propagate along the edges of the sample. These edge states, termed chiral edge states, propagate unidirectionally along the edge. Consequently, QAHI is distinguished by a quantized Hall effect, even in the absence of external magnetic fields. The existence of QAHI states has been theoretically predicted in a range of materials [5–7] and experimentally verified in Cr-doped

topological insulator films for the first time [8]. Subsequently, QAHI has been experimentally demonstrated in various materials, including Cr-doped $(Bi, Sb)_2Te_3$ films [9–17], V-doped $(Bi, Sb)_2Te_3$ films [10,18–22], $MnBi_2Te_4$ [23–25], and recently, moiré superlattice systems [26–28]. Remarkably, the proximity of a QAHI to an s-wave superconductor (SC) was predicted to potentially realize a chiral topological superconductor within these heterostructures via the superconducting proximity effect [29,30]. Therefore, QAHI/SC heterostructures have garnered considerable attention as promising platforms for realizing topological superconductors [29,31–42]. More interestingly, when a QAHI is sandwiched by two QAHI/SC heterostructures, supercurrent is carried by the chiral edge states, termed a chiral Josephson junction (JJ) in our paper. Investigating JJs based on QAHIs provides insight into the interplay between topology and superconductivity, offering the potential for novel phenomena and applications in quantum information processing and topological quantum computing [43–46].

Generally, the supercurrent in JJs is generated by the Andreev reflection process, which involves the conversion of an electron into a hole at the superconductor interface [47]. This process is accompanied by the creation of a Cooper pair in the superconducting region. As shown in Fig. 1(d), local Andreev reflections (LARs) occur uniformly in a conventional JJ. Thus,

*Contact author: qijj@baqis.ac.cn
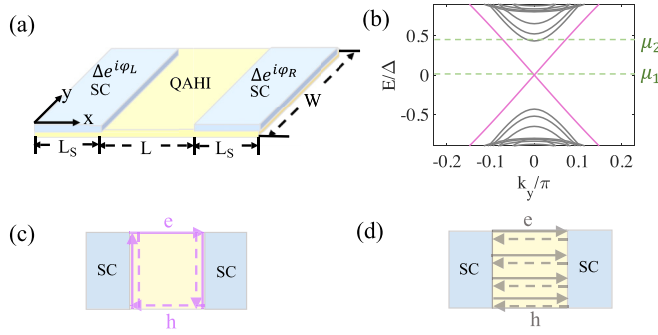†Contact author: czchen@suda.edu.cn

FIG. 1. (a) Schematic diagram of a QAHI-based JJ. The QAHI is partially covered by two superconducting electrodes, both composed of QAHI/SC heterostructures. The central region and the superconducting region have sizes of $W \times L$ and $W \times L_s$, respectively. (b) The QAHI energy spectrum with a length of $L = 40a$ is calculated using a lattice model described by Eq. (2). $\mu_1 = 0$ and $\mu_2 = 0.42\Delta$ are the chemical potentials, indicated by the green dashed lines. (c) Schematic diagram of CARs in real space, where Andreev pairs are constituted by electrons and holes propagating along opposing edges. (d) Schematic diagram of LARs in real space, where Andreev pairs formed by bulk carriers exhibit uniform distribution within the central region. In (b)–(d), we use purple (gray) lines to represent edge (bulk) carriers, respectively.

the critical Josephson current I_c, which is carried by bulk carriers, oscillates with the external magnetic flux Φ due to the interference of the supercurrents flowing through the junction in the presence of the magnetic flux. This oscillatory behavior gives rise to a quantum interference pattern known as the Fraunhofer pattern. The Fraunhofer pattern is characterized by a central lobe with a width of $2\Phi_0$ and decaying side lobes. Here, $\Phi_0 = h/2e$ is the flux quantum, h the Planck constant, and e the electron charge. When time-reversal symmetry is preserved, the Fraunhofer pattern is symmetric, meaning $I_c(\Phi) = I_c(-\Phi)$.

On the other hand, in a chiral JJ depicted in Fig. 1(a), the presence of gapped bulk states inhibits the bulk supercurrent. However, supercurrents can propagate through the chiral edge states even when the chemical potential resides within the bulk gap. Due to the chiral nature of edge states, electrons on the top edge are transformed into holes propagating along the bottom edge [see Fig. 1(c)]. This conversion of electrons and holes takes place in the spatially separated edges, known as crossed Andreev reflections (CARs) [48–52]. This process is reminiscent of the Aharonov-Bohm (AB) oscillations [53], where electrons traveling along different paths enclose a magnetic flux Φ, causing resistance to oscillate with the magnetic flux exhibiting a periodicity of $2\Phi_0$ [54]. Consequently, the critical Josephson current I_c in response to the external magnetic flux Φ can be described theoretically by the periodicity of $2\Phi_0$ [48,49,52,55–59]. On the other hand, experimental observations have confirmed the importance of the bulk states, induced by magnetic dopants, on the transport properties of QAHIs [2,3]. However, previous studies did not consider the effects of these bulk states on the quantum interference patterns in chiral JJs. Therefore, research addressing this question is highly desirable.

In this work, we systematically explore a JJ based on a QAHI with magnetic dopants, aiming to address the above question. The Josephson current I_s is calculated by the recursive Green-function method. First, we present the critical Josephson current I_c as a function of the magnetic flux Φ for various chemical potentials μ. We find an evolution of quantum interference patterns from a $2\Phi_0$-periodic oscillation pattern to an asymmetric Fraunhofer pattern. The two typical interference patterns result from different Andreev reflection processes as shown in Figs. 1(c) and 1(d). Second, we simulate the effects of magnetic domains on the two interference patterns. We find that the asymmetric Fraunhofer pattern is very robust against the domains, while the $2\Phi_0$-periodic oscillation pattern is susceptible to modest magnetic fluctuations. Remarkably, a different Fraunhofer-like pattern, with periods twice those of the conventional one, emerges when the chiral edge state and magnetic domain states coexist at $\mu = 0$. The observed Fraunhofer-like pattern is expected to extend beyond our model and could be prevalent in materials doped with magnetic impurities, suggesting potential for further experimental verification.

The paper is organized as follows. We introduce the model and methods employed in this work in Sec. II. Section III presents the key findings of our calculations and the corresponding remarks. More specifically, Sec. III A discusses two distinct quantum interference patterns. The effects of magnetic domains, which are covered in Sec. III B, inevitably occur in the magnetically doped topological insulators. We find that the $2\Phi_0$-periodic oscillation effect is destroyed by modest magnetic fluctuations. A different Fraunhofer-like pattern is observed even when $\mu = 0$. Section IV is the conclusion.

II. MODEL AND METHODS

As depicted in Fig. 1(a), the QAHI-based junction comprises three parts: two superconducting electrodes and a central region with QAHI. The 4×4 low-energy effective Hamiltonian describing magnetic topological insulator thin films in the central region is given by [7,60]

$$H(\mathbf{k}) = \hbar v_F(k_y \sigma_x \tau_z - k_x \sigma_y \tau_z) + m(\mathbf{k})\tau_x + M_z \sigma_z \quad (1)$$

in the basis of $\psi_\mathbf{k} = [\psi_{\mathbf{k},t\uparrow}, \psi_{\mathbf{k},t\downarrow}, \psi_{\mathbf{k},b\uparrow}, \psi_{\mathbf{k},b\downarrow}]^T$ with the wave vector $\mathbf{k}$. $\uparrow$ ($\downarrow$) represents the spin direction, and t (b) denotes the top (bottom) layer. The symbols $\sigma_{x,y,z}$ and $\tau_{x,y,z}$ correspond to the Pauli matrices for spin and layer, respectively. M_z represents the exchange field along the z axis induced by the ferromagnetic ordering. The term $m(\mathbf{k}) = m_0 - m_1 \mathbf{k}^2$ describes the coupling between the top and bottom layers. The system is in the QAHI phase with the Chern number $C = \text{sgn}(M_z)$ when $|M_z| > |m_0|$, while it is a normal insulator with $C = 0$ when $|M_z| < |m_0|$.

In our numerical simulations, we discrete the Hamiltonian in Eq. (1) to a tight-binding model in a square lattice as [44]

$$H = \sum_{ij} (\psi_i^\dagger t_0 \psi_i + \psi_i^\dagger t_x \psi_{i+\hat{x}} + \psi_i^\dagger t_y \psi_{i+\hat{y}} + \text{H.c.}), \quad (2)$$

where $\hat{x}$ ($\hat{y}$) is the unit vector along the x (y) axis and i is the site index. The 4×4 matrices $t_{0,x,y}$ are given by

$$t_0 = \left(m_0 - 4\frac{m_1}{a^2}\right)\tau_x\sigma_0 + M_z\tau_0\sigma_z,$$

$$t_x = \left(\frac{m_1}{a^2}\tau_x\sigma_0 + \frac{iv_F}{2a}\tau_z\sigma_y\right)e^{i\phi_{i,i+\hat{x}}},$$

$$t_y = \frac{m_1}{a^2}\tau_x\sigma_0 - \frac{iv_F}{2a}\tau_z\sigma_x, \qquad (3)$$

where t_x gains a phase $\phi_{ij} = \pi \int_i^j \mathbf{A} \cdot d\mathbf{l}/\Phi_0$ due to the magnetic field B in the z direction with the vector potential $\mathbf{A} = (-yB, 0, 0)$, and $\Phi_0 = h/2e$ is the flux quantum with the Planck constant h and the elementary charge e. Here, σ_0 (τ_0) denotes the 2×2 identity matrix. The total magnetic flux of the central region is denoted as Φ. Utilizing Eqs. (2) and (3), we can visualize the energy spectrum in the QAHI when $\Phi = 0$, depicted in Fig. 1(b). The bulk states (gray) are gapped, accompanied by the gapless edge states (purple).

In proximity to an s-wave SC, a finite pair amplitude is induced in the QAHI. The Bogoliubov–de Gennes (BdG) Hamiltonian of QAHI/SC heterostructures in Nambu space is given by $H_{SC} = \sum_{\mathbf{k}} \Psi_{\mathbf{k}}^\dagger H_{SC}(\mathbf{k})\Psi_{\mathbf{k}}/2$ with $\Psi_{\mathbf{k}} = [(\Psi_{\mathbf{k},t\uparrow}, \Psi_{\mathbf{k},t\downarrow}, \Psi_{\mathbf{k},b\uparrow}, \Psi_{\mathbf{k},b\downarrow}), (\Psi_{-\mathbf{k},t\uparrow}^\dagger, \Psi_{-\mathbf{k},t\downarrow}^\dagger, \Psi_{-\mathbf{k},b\uparrow}^\dagger, \Psi_{-\mathbf{k},b\downarrow}^\dagger)]^T$, and

$$H_{SC}(\mathbf{k}) = \begin{pmatrix} H(\mathbf{k}) - \mu_s & \Delta \\ \Delta^\dagger & -H^*(-\mathbf{k}) + \mu_s \end{pmatrix},$$

$$\Delta = \begin{pmatrix} ie^{i\varphi_{L(R)}}\Delta_t\sigma_y & 0 \\ 0 & ie^{i\varphi_{L(R)}}\Delta_b\sigma_y \end{pmatrix}. \qquad (4)$$

Here, μ_s is the chemical potential of the superconducting regions, and φ_L and φ_R are the superconducting phases in the left and right sides of the junction. The physical properties only depend on the superconducting phase difference $\varphi = \varphi_L - \varphi_R$. Δ_t and Δ_b denote the induced superconducting pairing potentials on the top and bottom layers, respectively.

The QAHI regions in Nambu space can be represented as

$$H_{BdG}(\mathbf{k}) = \begin{pmatrix} H(\mathbf{k}) - \mu & 0 \\ 0 & -H^*(-\mathbf{k}) + \mu \end{pmatrix}. \qquad (5)$$

Here, μ is the chemical potential of the QAHI region. For simplicity, the parameters are set as follows: lattice constant $a = 1$, Fermi velocity $v_F = 1$, $\Delta_t = 0.5$ and $\Delta_b = 0$, $m_1 = 2\Delta_t a^2$, and $m_0 = -0.2\Delta_t$ in this work, and both the QAHI and superconducting regions have dimensions $W \times L(L_s) = 100a \times 40a$. In the following calculations, we use Δ instead of Δ_t.

The Josephson current I in the QAHI region can be calculated by the recursive Green-function method and expressed as [61–63]

$$I = -\frac{ieK_BT}{\hbar} \sum_n \text{Tr}[\hat{T}_x \hat{G}_{x+1,x}(i\omega_n) - \hat{T}_x^\dagger \hat{G}_{x,x+1}(i\omega_n)], \qquad (6)$$

where e is the electron charge, k_B is the Boltzmann constant, $\hbar$ is the reduced Planck constant, and T is the temperature. The hopping term $\hat{T}_x$ in Nambu space is given by $\hat{T}_x = \begin{pmatrix} t_x & \\ & -t_x^* \end{pmatrix}$,
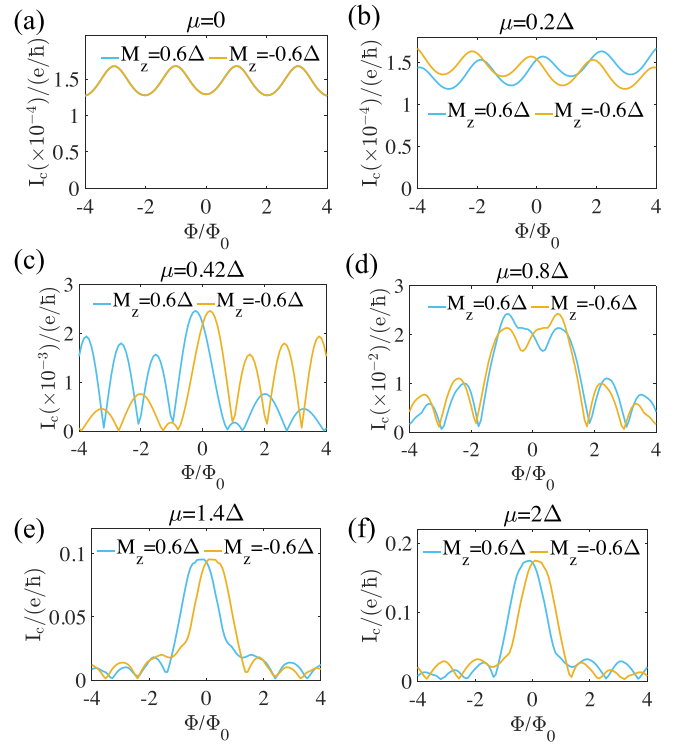

FIG. 2. Quantum interference patterns in different regimes. The critical Josephson current I_c vs the magnetic flux Φ in the unit of Φ_0. (a) CARs happen when only chiral edge states are included with $\mu = 0$. I_c exhibits the AB oscillation characterized by a periodicity of $2\Phi_0$. (b)–(e) The behavior of I_c deviates from the $2\Phi_0$-periodic oscillation as μ takes on values of 0.2Δ, 0.42Δ, 0.8Δ, and 1.4Δ, respectively. (c) LARs take place in the JJs, and the $2\Phi_0$-periodic oscillation is destroyed. (d) The emergence of central and side lobes is a consequence of the interference pattern transitioning toward a regime dominated by bulk carriers. (f) I_c displays the typical asymmetric Fraunhofer pattern with $\mu = 2\Delta$. In this regime, the bulk carriers uniformly flow through the whole QAHI region. In all cases, the blue (orange) solid lines represent I_c curves corresponding to $M_z = \pm0.6\Delta$, $\mu_s = \mu$, and the temperature $T = \Delta/200$.

where t_x originates from Eq. (3). The Green function is expressed as $\hat{G}(i\omega_n) = (i\omega_n - H_{BdG} - \Sigma_L - \Sigma_R)^{-1}$ with the Matsubara frequency $\omega_n = (2n + 1)\pi k_B T$. The index n in the sum represents a summation over Matsubara frequencies, where n spans all integer values. Here, $\Sigma_{L(R)}$ denotes the self-energy induced by the coupling between the left (right) superconducting leads and the QAHI region, which can be calculated numerically [64].

III. NUMERICAL RESULTS

A. Evolution of quantum interference patterns

In this section, we investigate the evolution of the quantum interference patterns within the QAHI-based junction as the chemical potential varies. At a chemical potential of $\mu = 0$, as depicted in Fig. 2(a), the QAHI region exclusively accommodates chiral edge carriers. At the interface between the QAHI and the SC, an electron from one chiral edge mode can tunnel into a hole on the opposite edge through the CAR process.

Similarly, the holes are then reflected as electrons along the other QAHI-SC interface. This entire process forms a loop, completing the transfer of the supercurrent, and leading to an intriguing AB oscillation pattern. This interference pattern, a hallmark of chiral edge states, exhibits two distinctive features: (1) Unlike the conventional Φ_0 periodicity, the critical Josephson current I_c has a periodicity of $2\Phi_0$. (2) The minima of I_c are nonzero. These findings align with prior research studies [48,49,52,55–59]. Furthermore, by shifting the chemical potential to $\mu = 0.2\Delta$, an observed phase shift arises from the finite chemical potential. This occurrence is tied to the sustenance of the Josephson current by Andreev bound states forming a closed loop. Consequently, the product of the Fermi wavelength and the circumference, $k_F * L_d$, introduces a phase shift, resulting in current oscillations relative to the chemical potential. The results depicted in Figs. 2(a) and 2(b) demonstrate that nonvanishing supercurrent can be sustained by the chiral edge states even in the absence of bulk carriers, exhibiting a periodicity of $2\Phi_0$. Such a supercurrent feature of the chiral edge state is very distinct from the behaviors of bulk states in the conventional JJs. Interestingly, when μ is 0.42Δ, the chemical potential touches with the bottom of the conduction band [see Fig. 1(b)]. Thus, bulk carriers begin to participate in the transport process, leading to the disruption of the $2\Phi_0$-periodic oscillation.

To trace the evolution of the Josephson current from edge states to the bulk further, we continue to increase the chemical potential to $\mu > 0.42\Delta$, disrupting the previously observed $2\Phi_0$ periodicity. Interestingly, the Fraunhofer pattern with a distinct central peak of width $2\Phi_0$ forms when $\mu > 0.8\Delta$ [Figs. 2(d)–2(f)], signaling the increased dominance of bulk states in the transport process. This occurrence correlates with the population of bulk carriers within the QAHI region, leading to a consistent appearance of LARs at QAHI-SC interfaces as μ increases [refer to Fig. 1(d)]. Due to the increase in bulk carriers, a noticeable enhancement in the maxima of I_c is also observed, as seen in Figs. 2(a)–2(f), exceeding hundreds of times. Furthermore, the Fraunhofer pattern displays an asymmetric feature due to broken time-reversal symmetry, namely, $I_c(M_z, \Phi) \neq I_c(M_z, -\Phi)$ when the magnetic field direction is reversed. Besides, the inversion symmetry invariance of the QAHI's Hamiltonian $H(\mathbf{k})$ leads to the relationship $I_c(M_z, \Phi) = I_c(-M_z, -\Phi)$ [65,66]. The inversion symmetry holds because $\mathcal{P}H(-\mathbf{k})\mathcal{P}^{-1} = H(\mathbf{k})$ with $\mathcal{P} = \sigma_z \tau_0$, where σ_z and τ_0 are the Pauli matrix and the unit matrix in spin space and layer space, respectively. In the subsequent calculations, we focus exclusively on the scenario where $M_z = 0.3$ due to the aforementioned relationship between $I_c(M_z)$ and $I_c(-M_z)$. In summary, I_c of the QAHI-based JJs undergoes a transition from a $2\Phi_0$-periodic oscillation pattern to an asymmetric Fraunhofer pattern by tuning the chemical potential μ. Note that we do not discuss the case where the chemical potentials μ and μ_s are different here because the periodicity of $2\Phi_0$ remains consistent when the difference is not large (see Appendix for more information).

To further reveal the origin of different interference patterns, we investigate the distribution of current j_c in the QAHI region when the total current has its maximum value [61–63]. The local critical current is usually used to repre-
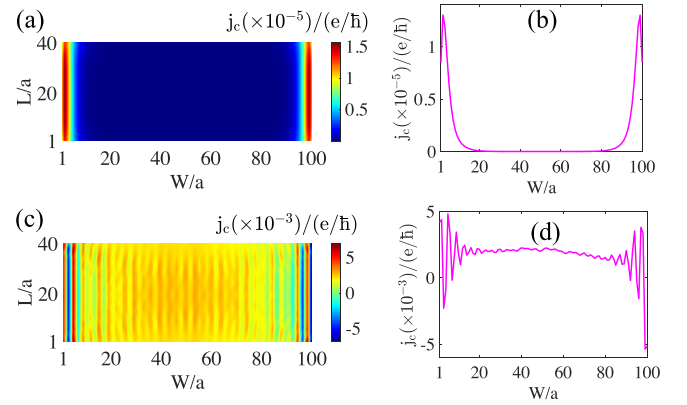

FIG. 3. The spatial distribution of current (a and c) in the QAHI region and (b and d) at the QAHI-SC interface when the total current at its maximum value is examined under varying chemical potentials: (a and b) $\mu = 0$ and (c and d) 2Δ. In all cases, $M_z = 0.6\Delta$, $\Phi = 0$, $\mu_s = \mu$, and the temperature $T = \Delta/200$.

sent the current distribution of various systems, e.g., quantum Hall systems [67]. Figure 3 demonstrates the distribution of current along the x direction, $j_c(y)$, corresponding to the superconducting phase difference φ, precisely when the total current $\sum_{y=1}^{W} j_c(y)$ reaches its maximum. At $\mu = 0$, the current predominantly flows along the QAHI region's two edges, as evidenced in the spatial distribution of j_c displayed in Figs. 3(a) and 3(b). This observation aligns with the phenomenon depicted in Fig. 1(c), where transport within the central region is solely governed by the propagation of chiral edge carriers. Additionally, this distribution of current is consistent with the quantum interference pattern shown in Fig. 2(a), characterized by a periodicity of $2\Phi_0$. Moreover, Figs. 3(c) and 3(d) show a bulk-dominated transport process, as the μ value is increased to 2Δ. Thus, local Andreev pairs become uniformly distributed across the QAHI region [see Fig. 1(d)], resulting in a Fraunhofer pattern, as observed in Fig. 2(f).

B. Effects of magnetic domains

Given the inevitable appearance of domains in magnetically doped topological insulators, we utilize a percolation model to simulate the effects of random domains on quantum interference patterns [68]. In realistic samples, domains typically exhibit irregular shapes. However, the specific shapes of domains are not of particular importance to our study. The bulk carriers induced by domains that are essential to the physics discussed in this section. Therefore, for the sake of simplicity, we model domains as rectangular in shape.

Figure 4(a) demonstrates the division of the central region into multiple blocks, each consisting of specific unit cells sized $d_1 \times d_2$. The magnetization within each block is randomly chosen to potentially flip with a probability of P, while the flipped magnetization strength is uniformly distributed in the range of $[-w/2, w/2]$ with the disorder strength w.

In Figs. 4(b) and 4(c), we display the domain-averaged critical Josephson current, denoted as $\bar{I}_c$. Initially, focusing on the case with $\mu = 0$ in Fig. 4(b), it is observed that $\bar{I}_c$ remains relatively stable [in comparison with Fig. 2(a)] when
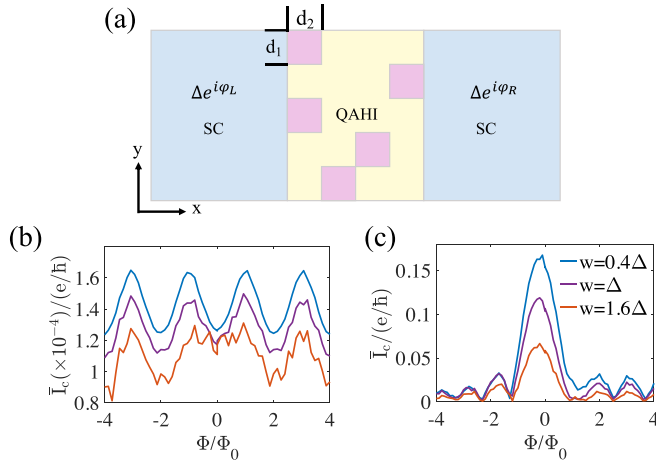
FIG. 4. (a) Schematic diagram of a QAHI-based JJ with a random magnetic domain structure (top view). The domain size is denoted by $d_1 \times d_2$. The quantum interference patterns are affected by the different strengths of magnetic disorder w when (b) $\mu = 0$ and (c) $\mu = 2\Delta$. In all cases, the domain size is $d_1 \times d_2 = 10a \times 4a$, and the domain probability $P = 0.5$. The remaining parameters are set as $M_z = 0.6\Delta$, $\mu_s = \mu$, and the temperature $T = \Delta/200$. We average over 50 random domain configurations [69].
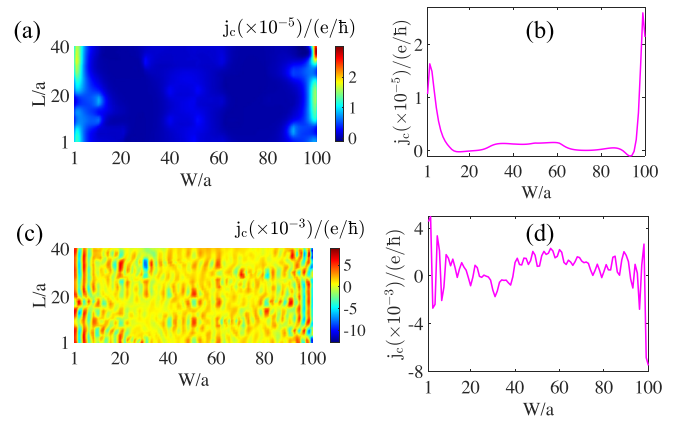

FIG. 5. The spatial distribution of current (a and c) in the QAHI region and (b and d) at the QAHI-SC interface when the total current has its maximum value affected by the domain structure is examined under varying chemical potential values: (a and b) $\mu = 0$ and (c and d) 2Δ. In this case, the domain size is $d_1 \times d_2 = 10a \times 4a$, the magnetic disorder strength $w = 1.6\Delta$, and the domain probability $P = 0.5$. In all cases, $M_z = 0.6\Delta$, $\Phi = 0$, $\mu_s = \mu$, and the temperature $T = \Delta/200$.

$w = 0.4\Delta$, indicating the robustness of chiral edge states against weak magnetic disorder (w). Then, at $w = \Delta$, the partial destruction of chiral edge modes diminishes the peak of the critical Josephson current $\bar{I}_c$. Despite domains causing the emergence of some bulk carriers in the QAHI region, the $2\Phi_0$ periodicity remains notably stable, owing to the dominance of transport by chiral edge modes. After that, increasing w to 1.6Δ initiates two simultaneous processes: the breakdown of chiral edge modes and a comparable contribution of bulk carriers to that of chiral edge carriers. Consequently, both the $2\Phi_0$ periodicity and the characteristic shape of the quantum interference pattern are lost. Conversely, at $\mu = 2\Delta$, we observe remarkable stability in the interference pattern of bulk carriers, maintaining the shape of the asymmetric Fraunhofer pattern even at $w = 1.6\Delta$. This suggests that the unconventional $2\Phi_0$-periodic oscillation is more susceptible to disruption compared to the resilient nature of the asymmetric Fraunhofer pattern under domain structures. Furthermore, the values of $\bar{I}_c$ gradually decrease with increasing w in Figs. 4(b) and 4(c), manifesting the influence of disorder effects.

Next, we examine the spatial distribution of current j_c within the QAHI region and at the QAHI-SC interface when the total current has its maximum value in Fig. 5, considering the existence of domain structures. In our calculation, we maintain a constant total magnetic flux $\Phi = 0$ and compute the distribution of current $j_c(y)$ along the x direction when the total current $\sum_{y=1}^{W} j_c(y)$ reaches its maximum. Due to the presence of domain structures, the distribution of current j_c exhibits static eddy-like currents in addition to constant currents. In Figs. 5(a) and 5(b) at $\mu = 0$, it is evident that the chiral edge modes are disrupted, and some bulk carriers emerge within the inner QAHI region due to the random distribution of domains across the QAHI region. This

observation aligns with the behavior depicted in the curve corresponding to $w = 1.6\Delta$ in Fig. 4(b). Conversely, when $\mu = 2\Delta$, the distribution of j_c exhibits characteristics akin to typical bulk transport, facilitating the stability of the asymmetric Fraunhofer pattern within domain structures. Notably, in Figs. 5(c) and 5(d), j_c values oscillate more prominently compared to Figs. 3(c) and 3(d).

To gain deeper insights into how domains affect the edge current, we explore the quantum interference pattern at $\mu = 0$ by varying the sizes of domains under a strong magnetic disorder strength $w = 2\Delta$, spanning a wider range of magnetic fields. In Fig. 6(a), an emergent central lobe is observed within the interval $\Phi/\Phi_0 \in (-2, 2)$, alongside side lobes at higher values of Φ. Additionally, the increase in the maxima of the central lobe is linked to the emergence of bulk carriers caused by a limited number of domains, particularly when the domain size is $d_1 \times d_2 = 50a \times 20a$. This interference pattern remarkably resembles the Fraunhofer pattern illustrated in Fig. 2(f). The emergence of bulk carriers in the QAHI region due to the presence of domains is the underlying cause of this phenomenon. When we decrease the domain size to $d_1 \times d_2 = 20a \times 10a$ to allow for a larger quantity of domains, a more distinct Fraunhofer-like pattern is evident within the $\bar{I}_c$ values in Fig. 6(b). Again, the presence of bulk carriers contributes to the enhancement of maxima of the central lobe, compared to the scenario depicted in Fig. 2(a). When the domain size is further decreased to $d_1 \times d_2 = 10a \times 4a$, as depicted in Fig. 6(c), the increased visibility of the periodicity in the higher lobes reveals a distinct Fraunhofer-like pattern. In particular, the periods of the central and side lobes are twice those of the conventional Fraunhofer pattern. To conclude, the observed Fraunhofer-like pattern in chiral JJs likely extends beyond our model and is prevalent in those doped with magnetic impurities, holding promise for further experimental verification. In summary, the interference pattern within the
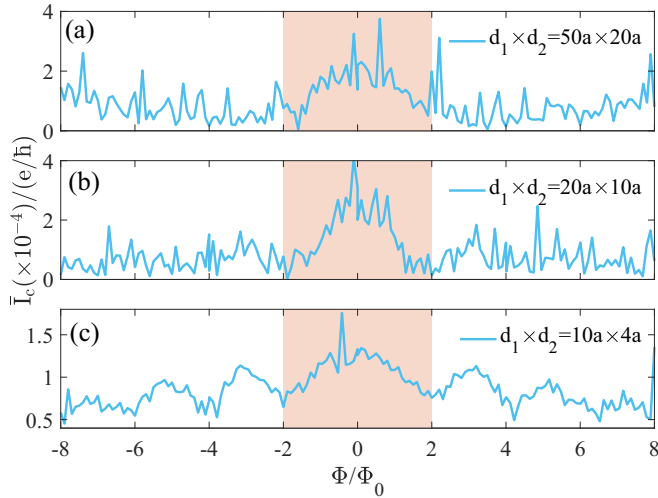
FIG. 6. The Fraunhofer-like patterns. The quantum interference patterns are affected by the domain structure at $\mu = 0$ in a larger magnetic field range with different block sizes $d_1 \times d_2$: (a) $50a \times 20a$, (b) $20a \times 10a$, and (c) $10a \times 4a$. In all cases, the magnetic disorder strength $w = 2\Delta$ and the domain probability $P = 0.5$. The remaining parameters are set as $M_z = 0.6\Delta$, $\mu_s = \mu$, and the temperature $T = \Delta/200$. In (a)–(c), the orange regions show the central lobes of the Fraunhofer-like pattern. We average over 15, 25, and 50 random domain configurations in (a), (b), and (c), respectively.

domain structure can be influenced by factors such as magnetic disorder strength w and domain size $d_1 \times d_2$.

IV. DISCUSSION AND CONCLUSION

While QAHIs can manifest in various material classes, our work focuses exclusively on magnetically doped topological insulators. The lack of comprehensive experimental results on QAHI-based JJs is primarily due to the significant experimental challenges. This challenge arises from the difficulty of achieving coexistence among the QAHI and superconductivity. Specifically, realizing the QAHIs requires magnetic doping within topological insulators. Although magnetic dopants are crucial for realizing QAHI, they also pose challenges for maintaining superconductivity. Therefore, achieving an appropriate magnetic doping ratio is crucial in experimental setups. Additionally, the presence of magnetic dopants raises questions regarding the formation of domains, which is one of the primary aspects addressed in our work. This results in the appearance of the anomalous Fraunhofer-like pattern, which is likely widespread in chiral JJs doped with magnetic impurities.

In this work, we explore the transport properties of the chiral JJs based on the QAHIs connecting to two superconducting electrodes, through numerical calculation of the Josephson current (I_c). We present a systematic transition from edge-state to bulk-state dominated supercurrent as the chemical potential varies. This transition leads to an evolution from a
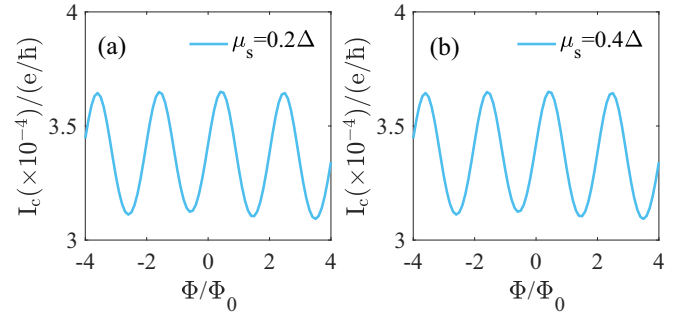

FIG. 7. Quantum interference patterns when the chemical potentials μ and μ_s exhibit differences. The critical Josephson current I_c vs the magnetic flux Φ in the unit of Φ_0 with varied chemical potentials in the superconducting regions: (a) $\mu_s = 0.2\Delta$ and (b) $\mu_s = 0.4\Delta$. In all subplots, we take $\mu = 0$, and the remaining parameters are consistent with those in Fig. 3(a) in the main text.

$2\Phi_0$-periodic oscillation pattern to an asymmetric Fraunhofer pattern. Furthermore, we observe the emergence of a different Fraunhofer-like pattern, characterized by periods twice those of the conventional pattern. This emergence is attributed to the coexistence of chiral edge states and bulk states induced by magnetic domains, even when the chemical potential is within the gap. This phenomenon is likely widespread in chiral JJs doped with magnetic impurities. Our findings also hold promise for direct experimental verification.

APPENDIX: THE EFFECTS OF THE MISMATCH BETWEEN μ AND μ_s

We investigate the effects of the mismatch between μ and μ_s on the quantum oscillation patterns. It should be pointed out that the mismatch in chemical potentials alters the scattering probability of Andreev reflections, potentially resulting in three aspects: (1) deviations from the periodicity of $2\Phi_0$, (2) the maxima of the critical current occurring not at $\Phi = \pm(2n + 1)\Phi_0$, where n is an integer, and (3) variations in the values of the critical currents. However, it should be emphasized that when the difference between μ and μ_s is not large, the periodicity of $2\Phi_0$ remains very steady, as illustrated in Fig. 7. Consequently, we set $\mu_s = \mu$ in the main text.

[1] F. D. M. Haldane, Model for a quantum Hall effect without Landau levels: Condensed-matter realization of the 'parity anomaly," Phys. Rev. Lett. **61**, 2015 (1988).

[2] C.-X. Liu, S.-C. Zhang, and X.-L. Qi, The quantum anomalous Hall effect: Theory and experiment, Annu. Rev. Condens. Matter Phys. **7**, 301 (2016).

[3] C.-Z. Chang, C.-X. Liu, and A. H. MacDonald, *Colloquium:* Quantum anomalous Hall effect, Rev. Mod. Phys. **95**, 011002 (2023).

[4] R. Chen, H.-P. Sun, B. Zhou, and D.-H. Xu, Chiral edge state coupling theory of transport in quantum anomalous Hall insulators, Sci. China Phys. Mech. Astron. **66**, 287211 (2023).

[5] C.-X. Liu, X.-L. Qi, X. Dai, Z. Fang, and S.-C. Zhang, Quantum anomalous Hall effect in $Hg_{1-y}Mn_yTe$ quantum wells, Phys. Rev. Lett. **101**, 146802 (2008).

[6] X.-L. Qi, T. L. Hughes, and S.-C. Zhang, Topological field theory of time-reversal invariant insulators, Phys. Rev. B **78**, 195424 (2008).

[7] R. Yu, W. Zhang, H. J. Zhang, S. C. Zhang, X. Dai, and Z. Fang, Quantized anomalous Hall effect in magnetic topological insulators, Science **329**, 61 (2010).

[8] C.-Z. Chang *et al.*, Experimental observation of the quantum anomalous Hall effect in a magnetic topological insulator, Science **340**, 167 (2013).

[9] M. Mogi, R. Yoshimi, A. Tsukazaki, K. Yasuda, Y. Kozuka, K. S. Takahashi, M. Kawasaki, and Y. Tokura, Magnetic modulation doping in topological insulators toward higher-temperature quantum anomalous Hall effect, Appl. Phys. Lett. **107**, 182401 (2015).

[10] Y. Ou, C. Liu, G. Jiang, Y. Feng, D. Zhao, W. Wu, X.-X. Wang, W. Li, C. Song, L.-L. Wang, W. Wang, W. Wu, Y. Wang, K. He, X.-C. Ma, and Q.-K. Xue, Enhancing the quantum anomalous Hall effect by magnetic codoping in a topological insulator, Adv. Mater. **30**, 1703062 (2018).

[11] J. G. Checkelsky, R. Yoshimi, A. Tsukazaki, K. S. Takahashi, Y. Kozuka, J. Falson, M. Kawasaki, and Y. Tokura, Trajectory of the anomalous Hall effect towards the quantized state in a ferromagnetic topological insulator, Nat. Phys. **10**, 731 (2014).

[12] X. Kou, S.-T. Guo, Y. Fan, L. Pan, M. Lang, Y. Jiang, Q. Shao, T. Nie, K. Murata, J. Tang, Y. Wang, L. He, T.-K. Lee, W.-L. Lee, and K. L. Wang, Scale-invariant quantum anomalous Hall effect in magnetic topological insulators beyond the two-dimensional limit, Phys. Rev. Lett. **113**, 137201 (2014).

[13] A. J. Bestwick, E. J. Fox, X. Kou, L. Pan, K. L. Wang, and D. Goldhaber-Gordon, Precise quantization of the anomalous Hall effect near zero magnetic field, Phys. Rev. Lett. **114**, 187201 (2015).

[14] A. Kandala, A. Richardella, S. Kempinger, C.-X. Liu, and N. Samarth, Giant anisotropic magnetoresistance in a quantum anomalous Hall insulator, Nat. Commun. **6**, 7434 (2015).

[15] E. O. Lachman, A. F. Young, A. Richardella, J. Cuppens, H. R. Naren, Y. Anahory, A. Y. Meltzer, A. Kandala, S. Kempinger, Y. Myasoedov, M. E. Huber, N. Samarth, and E. Zeldov, Visualization of superparamagnetic dynamics in magnetic topological insulators, Sci. Adv. **1**, e1500740 (2015).

[16] M. Liu, W. Wang, A. R. Richardella, A. Kandala, J. N. Li, A. Yazdani, N. Samarth, and N. P. Ong, Large discrete jumps observed in the transition between Chern states in a ferromagnetic topological insulator, Sci. Adv. **2**, e1600167 (2016).

[17] M. Kawamura, R. Yoshimi, A. Tsukazaki, K. S. Takahashi, M. Kawasaki, and Y. Tokura, Current-driven instability of the quantum anomalous Hall effect in ferromagnetic topological insulators, Phys. Rev. Lett. **119**, 016803 (2017).

[18] C.-Z. Chang, W. Zhao, D. Y. Kim, H. Zhang, B. A. Assaf, D. Heiman, S.-C. Zhang, C. Liu, M. H. Chan, and J. S. Moodera, High-precision realization of robust quantum anomalous Hall state in a hard ferromagnetic topological insulator, Nat. Mater. **14**, 473 (2015).

[19] C.-Z. Chang, W. Zhao, D. Y. Kim, P. Wei, J. K. Jain, C. Liu, M. H. W. Chan, and J. S. Moodera, Zero-field dissipationless chiral edge transport and the nature of dissipation in the quantum anomalous Hall state, Phys. Rev. Lett. **115**, 057206 (2015).

[20] S. Grauer, S. Schreyeck, M. Winnerlein, K. Brunner, C. Gould, and L. W. Molenkamp, Coincidence of superparamagnetism and perfect quantization in the quantum anomalous Hall state, Phys. Rev. B **92**, 201304(R) (2015).

[21] S. Grauer, K. M. Fijalkowski, S. Schreyeck, M. Winnerlein, K. Brunner, R. Thomale, C. Gould, and L. W. Molenkamp, Scaling of the quantum anomalous Hall effect as an indicator of axion electrodynamics, Phys. Rev. Lett. **118**, 246801 (2017).

[22] G. Lippertz, A. Bliesener, A. Uday, L. M. C. Pereira, A. A. Taskin, and Y. Ando, Current-induced breakdown of the quantum anomalous Hall effect, Phys. Rev. B **106**, 045419 (2022).

[23] Y. Deng, Y. Yu, M. Z. Shi, Z. Guo, Z. Xu, J. Wang, X. H. Chen, and Y. Zhang, Quantum anomalous Hall effect in intrinsic magnetic topological insulator $MnBi_2Te_4$, Science **367**, 895 (2020).

[24] Y. Gong *et al.*, Experimental realization of an intrinsic magnetic topological insulator, Chin. Phys. Lett. **36**, 076801 (2019).

[25] M. M. Otrokov *et al.*, Prediction and observation of an antiferromagnetic topological insulator, Nature (London) **576**, 416 (2019).

[26] A. L. Sharpe, E. J. Fox, A. W. Barnard, J. Finney, K. Watanabe, T. Taniguchi, M. Kastner, and D. Goldhaber-Gordon, Emergent ferromagnetism near three-quarters filling in twisted bilayer graphene, Science **365**, 605 (2019).

[27] M. Serlin, C. L. Tschirhart, H. Polshyn, Y. Zhang, J. Zhu, K. Watanabe, T. Taniguchi, L. Balents, and A. F. Young, Intrinsic quantized anomalous Hall effect in a moiré heterostructure, Science **367**, 900 (2020).

[28] T. Li, S. Jiang, B. Shen, Y. Zhang, L. Li, Z. Tao, T. Devakul, K. Watanabe, T. Taniguchi, L. Fu, J. Shan, and K. F. Mak, Quantum anomalous Hall effect from intertwined moiré bands, Nature (London) **600**, 641 (2021).

[29] X.-L. Qi and S.-C. Zhang, Topological insulators and superconductors, Rev. Mod. Phys. **83**, 1057 (2011).

[30] J. Wang, Q. Zhou, B. Lian, and S.-C. Zhang, Chiral topological superconductor and half-integer conductance plateau from quantum anomalous Hall plateau transition, Phys. Rev. B **92**, 064520 (2015).

[31] A. Uday, G. Lippertz, K. Moors, H. F. Legg, A. Bliesener, L. M. C. Pereira, A. A. Taskin, and Y. Ando, Induced superconducting correlations in the quantum anomalous Hall insulator, arXiv:2307.08578.

[32] M. Kayyalha1, D. Xiao, R. Zhang, J. Shin, J. Jiang, F. Wang, Y.-F. Zhao, R. Xiao, L. Zhang, K. M. Fijalkowski, P. Mandal, M. Winnerlein, C. Gould, Q. Li, L. W. Molenkamp, M. H. W. Chan, N. Samarth, and C.-Z. Chang, Absence of evidence for chiral Majorana modes in quantum anomalous Hall-superconductor devices, Science **367**, 64 (2020).

[33] H. Yi *et al.*, Interface-induced superconductivity in magnetic topological insulator-iron chalcogenide heterostructures, arXiv:2312.04353.

[34] L. Fu and C. L. Kane, Superconducting proximity effect and Majorana fermions at the surface of a topological insulator, Phys. Rev. Lett. **100**, 096407 (2008).

[35] X.-L. Qi, T. L. Hughes, and S.-C. Zhang, Chiral topological superconductor from the quantum Hall state, Phys. Rev. B **82**, 184516 (2010).

[36] J. Alicea, New directions in the pursuit of Majorana fermions in solid state systems, Rep. Prog. Phys. **75**, 076501 (2012).

[37] C. W. J. Beenakker, Search for Majorana fermions in superconductors, Annu. Rev. Condens. Matter Phys. **4**, 113 (2013).

[38] M. Sato and Y. Ando, Topological superconductors: A review, Rep. Prog. Phys. **80**, 076501 (2017).

[39] A. Yazdani, F. von Oppen, B. I. Halperin, and A. Yacoby, Hunting for Majoranas, Science **380**, eade0850 (2023).

[40] N.-X. Yang, Q. Yan, and Q.-F. Sun, Half-integer quantized thermal conductance plateau in chiral topological superconductor systems, Phys. Rev. B **105**, 125414 (2022).

[41] A. Ii, K. Yada, M. Sato, and Y. Tanaka, Theory of edge states in a quantum anomalous Hall insulator/spin-singlet *s*-wave superconductor hybrid system, Phys. Rev. B **83**, 224524 (2011).

[42] Y.-F. Zhou, Z. Hou, P. Lv, X. C. Xie, and Q.-F. Sun, Magnetic flux control of chiral Majorana edge modes in topological superconductor, Sci. China Phys. Mech. Astron. **61**, 127811 (2018).

[43] K. Sakurai, S. Ikegaya, and Y. Asano, Tunable-φ Josephson junction with a quantum anomalous Hall insulator, Phys. Rev. B **96**, 224514 (2017).

[44] Q. Yan, Y.-F. Zhou, and Q.-F. Sun, Anomalous Josephson current in quantum anomalous Hall insulator-based superconducting junctions with a domain wall structure, Chin. Phys. B **29**, 097401 (2020).

[45] R. Nakai, K. Nomura, and Y. Tanaka, Edge-induced pairing states in a Josephson junction through a spin-polarized quantum anomalous Hall insulator, Phys. Rev. B **103**, 184509 (2021).

[46] Q. Cheng, Q. Yan, and Q.-F. Sun, Spin-triplet superconductor-quantum anomalous Hall insulator-spin-triplet superconductor Josephson junctions: 0-π transition, ϕ_0 phase, and switching effects, Phys. Rev. B **104**, 134514 (2021).

[47] A. F. Andreev, The thermal conductivity of the intermediate state in superconductors, Sov. Phys. JETP **19**, 1228 (1964).

[48] A. Y. Zyuzin, Superconductor–normal-metal–superconductor junction in a strong magnetic field, Phys. Rev. B **50**, 323 (1994).

[49] J. A. M. van Ostaay, A. R. Akhmerov, and C. W. J. Beenakker, Spin-triplet supercurrent carried by quantum Hall edge states through a Josephson junction, Phys. Rev. B **83**, 195441 (2011).

[50] F. Dominguez, E. G. Novik, and P. Recher, Fraunhofer pattern in the presence of Majorana zero modes, arXiv:2210.02065.

[51] T. Haidekker Galambos, S. Hoffman, P. Recher, J. Klinovaja, and D. Loss, Superconducting quantum interference in edge state Josephson junctions, Phys. Rev. Lett. **125**, 157701 (2020).

[52] Z.-T. Sun, J.-X. Hu, Y.-M. Xie, and K. T. Law, Anomalous $h/2e$ periodicity and Majorana zero modes in chiral Josephson junctions, arXiv:2308.01079.

[53] Y. Aharonov and D. Bohm, Significance of electromagnetic potentials in the quantum theory, Phys. Rev. **115**, 485 (1959).

[54] R. A. Webb, S. Washburn, C. P. Umbach, and R. B. Laibowitz, Observation of $\frac{h}{e}$ Aharonov-Bohm, Phys. Rev. Lett. **54**, 2696 (1985).

[55] M. Ma and A. Y. Zyuzin, Josephson effect in the quantum Hall regime, Europhys. Lett. **21**, 941 (1993).

[56] D. S. Shapiro, A. Shnirman, and A. D. Mirlin, Current-phase relation and h/e-periodic critical current of a chiral Josephson contact between one-dimensional Majorana modes, Phys. Rev. B **93**, 155411 (2016).

[57] J. Liu, H. Liu, J. Song, Q.-F. Sun, and X. C. Xie, Superconductor-graphene-superconductor Josephson junction in the quantum Hall regime, Phys. Rev. B **96**, 045401 (2017).

[58] C.-Z. Chen, J. J. He, D.-H. Xu, and K. T. Law, Emergent Josephson current of $N = 1$ chiral topological superconductor in quantum anomalous Hall insulator/superconductor heterostructures, Phys. Rev. B **98**, 165439 (2018).

[59] Y. Alavirad, J. Lee, Z.-X. Lin, and J. D. Sau, Chiral supercurrent through a quantum Hall weak link, Phys. Rev. B **98**, 214504 (2018).

[60] J. Wang, B. Lian, and S. C. Zhang, Universal scaling of the quantum anomalous Hall plateau transition, Phys. Rev. B **89**, 085106 (2014).

[61] A. Furusaki, DC Josephson effect in dirty SNS junctions: Numerical study, Physica B: Condens. Matter **203**, 214 (1994).

[62] Y. Asano, Numerical method for dc Josephson current between *d*-wave superconductors, Phys. Rev. B **63**, 052512 (2001).

[63] Y. Asano, Y. Tanaka, M. Sigrist, and S. Kashiwaya, Josephson current in *s*-wave-superconductor/Sr_2RuO_4 junctions, Phys. Rev. B **67**, 184505 (2003).

[64] T. Ando, Quantum point contacts in magnetic fields, Phys. Rev. B **44**, 8017 (1991).

[65] K. Saitoh, S. Kashiwaya, H. Kashiwaya, Y. Mawatari, Y. Asano, Y. Tanaka, and Y. Maeno, Inversion symmetry of Josephson current as test of chiral domain wall motion in Sr_2RuO_4, Phys. Rev. B **92**, 100504(R) (2015).

[66] S. Kashiwaya, K. Saitoh, H. Kashiwaya, M. Koyanagi, M. Sato, K. Yada, Y. Tanaka, and Y. Maeno, Time-reversal invariant superconductivity of Sr_2RuO_4 revealed by Josephson effects, Phys. Rev. B **100**, 094530 (2019).

[67] H. Li, H. Jiang, Q.-F. Sun, and X. C. Xie, Emergent energy dissipation in quantum limit, Sci. Bull. **69**, 1221 (2024).

[68] Y.-H. Li, J. Liu, H. Liu, H. Jiang, Q.-F. Sun, and X. C. Xie, Noise signatures for determining chiral Majorana fermion modes, Phys. Rev. B **98**, 045141 (2018).

[69] We do not conduct averaging over more samples. The main reason for this limitation is the significant challenge posed by the computational constraints in numerical simulations. Furthermore, the fluctuations observed in Figs. 5(b) and 6 result from insufficient ensemble averaging.